Available online at www.sciencedirect.com

ScienceDirect

Geochimica et Cosmochimica Acta 332 (2022) 124–137

Geochimica et Cosmochimica Acta

www.elsevier.com/locate/gca

Calcium diffusion in enstatite, with application to closure temperature of the Ca-in-opx thermometer

D.J. Cherniak [a,*], Y. Liang [c]

[a] Department of Earth and Environmental Sciences, Rensselaer Polytechnic Institute, Troy, NY 12180, USA
[c] Department of Earth, Environmental and Planetary Sciences, Brown University, Providence, RI 02912, USA

Received 24 June 2021; accepted in revised form 6 June 2022; Available online 25 June 2022

Abstract

Chemical diffusion of Ca has been characterized in natural enstatite under buffered conditions (IW, NNO) and in air. Experiments were conducted using synthesized powder sources, with Ca diffusion profiles measured with Rutherford Backscattering Spectrometry. A variety of sources of diffusant were used to investigate the effects of silica activity and Ca concentration on diffusion. Calcium diffusion appears relatively insensitive to crystallographic orientation and oxygen fugacity under the range of investigated conditions, and also appears little influenced by differences in silica activity and Ca concentration in the diffusant source. For Ca diffusion in a natural enstatite, we obtain the following Arrhenius relation for diffusion over the temperature range 750–1150 °C,

$$D = 1.17 \times 10^{-10} \exp(-240 \pm 10 \text{ kJ mol}^{-1}/RT) \text{ m}^2\text{sec}^{-1}.$$

Calcium diffusion is slower than Mg, Cr and Fe in enstatite, but faster than larger divalent cations Pb and Eu that also are likely to preferentially occupy the M2 site. Calcium diffusion is also faster than that for trivalent REE and tetravalent Ti in enstatite. Calcium diffusivities in enstatite are intermediate between Ca diffusivities in clinopyroxene and olivine, with Ca diffusion in enstatite about 2 orders of magnitude faster than Ca self-diffusion in diopside and 2 orders of magnitude slower than Ca diffusion in olivine.

Diffusion parameters obtained from this study were used to develop a simple model for closure temperature of the Ca-in-opx thermometer of Brey and Köhler (1990). By coupling closure temperature and the Ca-in-opx thermometer, it is possible to constrain cooling rates of peridotites and pyroxenites. Applications to peridotites from the Lanzo Massif and the Oman ophiolite are presented.

Keywords: Diffusion; Calcium; Pyroxene; Rutherford Backscattering; Thermometry

1. INTRODUCTION

Pyroxene is a major rock-forming mineral in the Earth's upper mantle and lower crust, and plays an important role in the generation and differentiation of mafic and ultramafic rocks in the Earth, Moon, Mars, and other planetary bodies. Orthopyroxene can incorporate and fractionate a variety of minor and trace elements at high temperature magmatic and subsolidus conditions. Calcium is a minor cation in the M2 site of orthopyroxene. The solubility of Ca in orthopyroxene decreases as a function of temperature, which can be used as a thermometer for peridotites and pyroxenites (e.g., Lindsley, 1983; Brey and Köhler, 1990). The interpretation of the calculated temperature depends on thermal history experienced by the peridotites and pyroxenites. For well-equilibrated peridotites from

* Corresponding author at: Department of Physics, University at Albany, Albany, NY 12222, USA.
E-mail addresses: dcherniak@albany.edu (D.J. Cherniak), yan_liang@brown.edu (Y. Liang).

https://doi.org/10.1016/j.gca.2022.06.018
0016-7037/

cratons, orthopyroxene grains in hand samples are chemically homogeneous. Temperatures calculated using Ca solubility-based thermometers represent equilibrium temperatures as they are generally in good agreement with temperatures derived from pyroxene thermometers that are based on Fe-Mg exchange in the pyroxenes or REE partitioning between orthopyroxene and clinopyroxene (e.g., Witt-Eickschen and O'Neill, 2005; Nimis and Grütter, 2010; Liang et al., 2013). For peridotites from tectonically perturbed or active regions, such as orogenic, ophiolitic, and abyssal peridotites, orthopyroxene grains are often chemically inhomogeneous with core-to-rim zoning in Ca, Al, Cr, Ti, Fe, Mg, and trace elements (e.g., Witt-Eickschen and Seck, 1991; Takazawa et al., 1996; Ozawa, 2004; Witt-Eickschen, 2007; Jollands and Müntener, 2019; Aoki et al., 2020). In general, Ca concentrations in orthopyroxene cores are higher than Ca concentrations in orthopyroxene rims, which can be attributed to diffusional loss of Ca to coexisting clinopyroxene during cooling. The amount of Ca retained in orthopyroxene cores depends on orthopyroxene grain size, cooling rate, and Ca diffusion in the orthopyroxene. Surprisingly, there is no data for Ca diffusion in orthopyroxene.

Significant progress has been made in characterizing diffusion coefficients of geochemically important major and trace elements (e.g., Mg, Cr, Ti, REE, and Pb) in orthopyroxene (e.g., Ganguly and Tazzoli, 1994; Schwandt et al., 1998; Cherniak, 2001; Dohmen et al., 2016; Cherniak and Liang, 2007, 2012; Ganguly et al., 2007; Sano et al., 2011). The purpose of this study is to provide data for Ca diffusion in orthopyroxene. Experiments characterizing Ca diffusion in a natural enstatite were conducted at 1 bar for a range of temperatures (750–1150 °C) and oxygen fugacity (from in air to the IW buffer) using a constant source method (Section 2). An Arrhenius relation for Ca diffusion in enstatite is obtained (Section 3) and compared with those for other cations in orthopyroxene (Section 4). The new diffusion parameters for Ca in enstatite are used to assess diffusional loss of Ca under isothermal and cooling conditions (Sections 5.1 and 5.2) and to develop a Dodson-like closure temperature model for the Ca-in-opx thermometer of Brey and Köhler (1990). As an initial application, we use the new closure temperature model and concentrations of Ca in orthopyroxene to infer cooling rates of peridotites from the Lanzo Massif and the Oman ophiolite (Sections 5.2 and 5.3).

2. EXPERIMENTAL METHODS

2.1. Materials and experimental procedure

Calcium diffusion experiments were run on a natural enstatite from Embilipitiya, Sri Lanka, the same enstatite used in studies of Pb (Cherniak, 2001), REE (Cherniak and Liang, 2007), and Ti diffusion (Cherniak and Liang, 2012). The enstatite composition is provided in Table 1. In terms of pyroxene structure unit, we have $Ca_{0.001}Mg_{1.927}Fe_{0.016}Al_{0.047}Ti_{0.0005}Si_{1.992}O_6$. Samples selected for experiments were optically clear and free of inclusions. Typical samples were square or rectangular,

Table 1
Compositional information on enstatite used in this study from Cherniak (2001).

	wt%
SiO_2	60.03
TiO_2	0.02
Al_2O_3	1.19
FeO	0.59
MnO	–
MgO	38.94
CaO	0.04
Cr_2O_3	–
Na_2O	–
total	100.81

2–5 mm on a side. Samples were oriented to measure diffusion parallel to c, and normal to (2 1 0) cleavage faces. Most samples were oriented to measure D normal to (2 1 0), but a few were cut to measure D normal to (0 0 1), as diffusion parallel to c is likely to be the fastest in orthopyroxene in cases where diffusional anisotropy exists (e.g., Ganguly and Tazzoli, 1994; Ganguly et al., 2007; Sano et al., 2011). All specimens were polished to 0.3 μm alumina, and finished with a chemical polish using a colloidal silica suspension. Following polishing, samples were cleaned ultrasonically in distilled water and ethanol. Samples were then pre-annealed under conditions comparable to those to be experienced during diffusion experiments, either in air or with solid buffers, following a procedure comparable to that of the experimental diffusion anneals described below, to equilibrate point defects prior to the diffusion experiments themselves.

Several different sources of diffusant were used for experiments. One diffusant source (source "b") used a powder source of diopside composition, made by combining dried MgO, SiO_2 and $CaSiO_3$ powders (in molar ratio 1:1:1), mixed under ethanol, dried and heated in a platinum crucible at 1300 °C for one day; this was diluted 1:5 (by wt) with a synthesized enstatite powder (made by solid-state reaction of a stoichiometric mix of dried MgO and SiO_2 powders, heated at 1200 °C for one day); the combined enstatite-diopside mixture was then heated for an additional day at 1200 °C. The two other diffusant sources (sources "c" and "d") explored the effect of different silica activities in the source material, using assemblages of the synthetic enstatite and diopside as prepared above, along with either SiO_2 or forsterite powders (both obtained from Alfa-Aesar). In these sources, one part (by wt) of either SiO_2 or forsterite was combined with six parts enstatite and three parts diopside powder, mixed thoroughly under ethanol, dried, and heated at 975 °C for several hours in a box furnace. In addition, some early experiments were conducted using the pure diopside source (made as described above). However, these experiments showed very high Ca concentrations so were not used in deriving diffusion data in this study.

Experiments were run either in air or under buffered conditions. To make a diffusion charge, the source and polished enstatite samples were placed in platinum capsules, which were crimped shut. For buffered experiments,

capsules prepared in this manner were then placed in silica glass ampoules along with a crimped platinum capsule containing either a mixture of iron flakes and FeO powder (to buffer at IW), or a mixture of Ni and NiO powders (to buffer at NNO). Inside the silica glass ampoules, silica glass chips were placed between the capsule containing the solid buffer and the capsule containing the source and sample to physically separate sample and buffer. The assemblies in the silica glass ampoules were then sealed under vacuum.

Prepared capsules were annealed in 1-atm tube furnaces for times ranging from a few hours to a few months at temperatures from 750 to 1150 °C. Experiments below 1100 °C were conducted in Kanthal wound vertical tube furnaces, with temperatures monitored with chromel–alumel (type K) thermocouples. Higher-temperature experiments were conducted in tube furnaces with $MoSi_2$ heating elements, with temperature monitored with Pt-Pt10%Rh (type S) thermocouples. Temperature uncertainties are ±2 °C in both cases. On completion of the diffusion anneals, samples were quenched by removing them from furnaces and permitting them to cool in air. Samples were then extracted from the capsules, freed of residual source material and cleaned ultrasonically in successive baths of distilled water and ethanol. SEM and BSE imaging of samples following diffusion anneals and cleaning show small numbers of cracks and pits, and only isolated fragments of material clinging to sample surfaces; given the distribution and composition of these materials (primarily an Fe-rich phase and noble metal from sample capsule materials) on the surface, they would have minimal effects on RBS analyses. Examples of sample surface images are included in the supplemental materials (Fig. S1).

2.2. RBS analysis

Rutherford Backscattering Spectrometry (RBS) has been used in numerous diffusion studies of pyroxene, including those on Pb (Cherniak, 1998, 2001) and Ti diffusion (Cherniak and Liang, 2012) in a range of pyroxene compositions, Sr diffusion in diopside (Sneeringer et al., 1984), Ca self-diffusion in diopside (Dimanov et al., 1996; Dimanov and Ingrin, 1995), and REE diffusion in enstatite (Cherniak and Liang, 2007). The analytical approach used here is comparable to that used in our previous diffusion studies for pyroxene (Cherniak, 1998, 2001; Cherniak and Liang, 2007, 2012), with $^4He^+$ incident beam energies ranging between 2 and 3 MeV for analysis. Beam spots were typically about 1 mm^2, and depth resolution ~10 nm. Spectra were converted to Ca concentration profiles employing procedures similar to those outlined in these publications, in this case taking into account the backgrounds in the energy region of interest in the spectra, primarily due to naturally present Fe and Ca in the samples. With this procedure, reported Ca concentrations in profiles and the data table are the relative concentrations with background Ca in the starting enstatite subtracted. The Ca concentration profiles (C) obtained from RBS spectra were fit with a model to determine the diffusion coefficient (D). Diffusion is modeled as simple one-dimensional, concentration independent diffusion in a semi-infinite medium with a source reservoir maintained at constant concentration (i.e., a complementary error function solution). The rationale for the use of this model has been discussed in previous publications (e.g., Cherniak and Watson, 1992, 1994). Diffusivities are evaluated by plotting the inverse of the error function (i.e., $\mathrm{erf}^{-1}((C_0 - C(x,t))/C_0)$) vs. depth ($x$) in the sample. A straight line of slope $(4Dt)^{-1/2}$ results if the data satisfy the conditions of the model. The surface concentration of diffusant (C_0), is independently determined by iteratively varying its value until the intercept of the line converges on zero. In Fig. 1, typical diffusion profiles and their inversions through the error function are shown. The uncertainties in concentration and depth from each data point [mainly derived from counting statistics and background (primarily due to the presence of Fe) in the former and detector resolution in the latter] were used to evaluate the uncertainties in the diffusivities determined from the fits to the model. Calcium concentrations at sample surfaces using the "b" source (1:5 ratio diopside:enstatite) range from 1000 to 5000 atomic ppm; Ca surface concentrations for the "c" and "d" sources are ~1000 ppm and 2000 ppm, respectively.

3. RESULTS

Results from the Ca diffusion experiments are presented in Table 2 and plotted in Fig. 2. The data show little evidence of strong anisotropy for Ca diffusion in enstatite (Fig. 2). In addition, diffusivities obtained with the 5:1 enstatite:diopside source ("b") are in agreement with those from experiments run with Di-En-Fo and Di-En-SiO_2 sources ("c" and "d"). The data show at most a weak, positive dependence of Ca diffusion on oxygen fugacity over the investigated range of conditions (Fig. 3). At 1050 °C, we have $D \propto (fO_2)^m$, where $m = 0.052 \pm 0.017$. However, the dependence on fO_2 diminishes at 850 °C (Fig. 3).

For diffusion normal to the (2 1 0) cleavage face, for experiments run in air over the temperature range 750–1150 °C, we obtain the following Arrhenius relation:

$$D = 2.18\times10^{-10}\exp\left(-245 \pm 11 \text{ kJ mol}^{-1}/RT\right) \text{ m}^2\text{sec}^{-1}$$
$$(\log D_0 = -9.66 \pm 0.46) \quad (1)$$

Similar diffusivities are found for diffusion normal to (0 0 1), suggesting little anisotropy of Ca diffusion in enstatite. A "global" fit to all data, incorporating all sources, orientations and buffer conditions, yields the following Arrhenius relation for Ca diffusion in enstatite:

$$D = 1.17\times10^{-10}\exp\left(-240 \pm 10 \text{ kJ mol}^{-1}/RT\right) \text{ m}^2\text{sec}^{-1}$$
$$(\log D_0 = -9.93 \pm 0.43) \quad (2)$$

Finally, a time-series study (Fig. 4), run at 950 °C, which shows consistent diffusivities over experimental durations differing by a factor of eight, suggests that the measured concentration profiles represent volume diffusion and are not a consequence of other phenomena such as surface reaction.

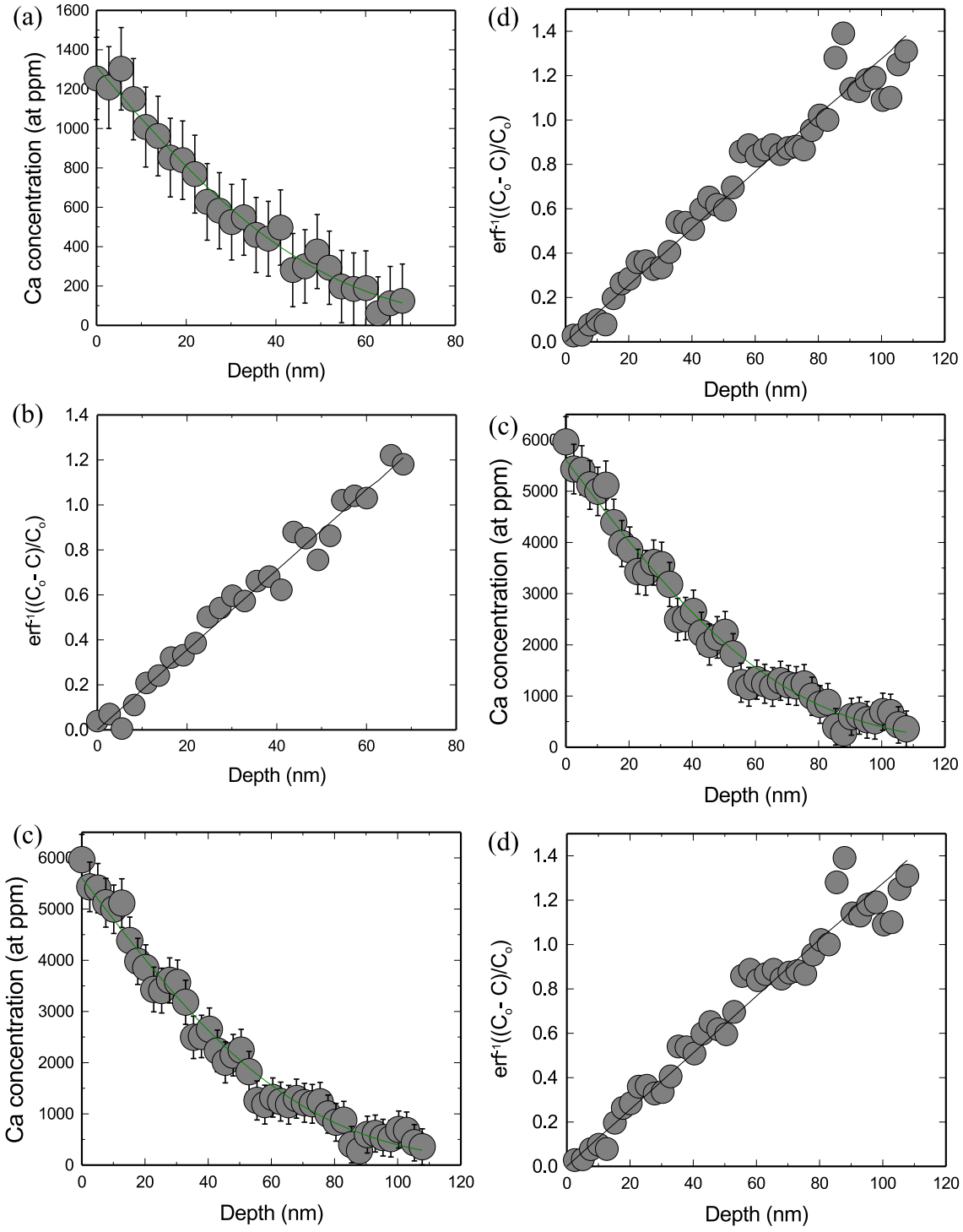

Fig. 1. Typical concentration profiles for Ca diffusion in natural enstatite from experiments, Ca-En-11 (a,b), CaEn-13 (c,d), and CaEn-30 (e, f). In (a). (c) and (e), the measured diffusion profile is plotted with complementary error function curves. In (b), (d) and (f), the data are linearized by inversion through the error function. The slope of the lines is equal to $(4Dt)^{-1/2}$. C is the Ca concentration at a given depth, and C_o is the Ca concentration at the pyroxene surface.

4. DISCUSSION

The temperature range of diffusion anneals in this study spans conditions for the orthoenstatite – protoenstatite structural transition, although it should be noted that we have relatively few data above this temperature. The potential for effects of this transition on diffusion has been discussed previously (Cherniak and Liang, 2007), but prior

Table 2
Ca Diffusion in Enstatite.

	T (°C)	time (sec)	D (m^2sec^{-1})	log D	±	source	buffer	surface conc (at ppm)*
Normal to (210)								
CaEn-18	748	2.91×10^{6}	1.65×10^{-22}	−21.78	0.29	b	air	1600
CaEn-14	800	2.15×10^{6}	2.62×10^{-22}	−21.58	0.14	b	air	2150
CaEn-11	851	6.62×10^{5}	1.20×10^{-21}	−20.92	0.18	b	air	1310
CaEn-19	850	5.80×10^{5}	8.62×10^{-22}	−21.06	0.31	b	NNO	2670
CaEn-20	850	5.80×10^{5}	8.56×10^{-22}	−21.07	0.33	b	IW	1800
CaEn-33	850	6.19×10^{5}	5.03×10^{-22}	−21.30	0.37	d	air	2040
CaEn-32	850	6.08×10^{5}	1.33×10^{-21}	−20.88	0.27	c	air	1750
CaEn-10	902	2.52×10^{5}	6.51×10^{-21}	−20.19	0.27	b	air	890
CaEn-16	950	1.48×10^{5}	9.63×10^{-21}	−20.02	0.29	b	air	1230
CaEn-21	950	6.08×10^{5}	2.13×10^{-21}	−20.67	0.14	b	air	2990
CaEn-24	950	7.92×10^{4}	5.09×10^{-21}	−20.29	0.20	b	air	2360
CaEn-25	949	2.52×10^{5}	2.01×10^{-21}	−20.67	0.27	b	NNO	1170
CaEn-26	949	2.52×10^{5}	3.77×10^{-21}	−20.42	0.16	b	IW	1600
CaEn-30	950	1.90×10^{5}	3.88×10^{-21}	−20.41	0.19	c	air	1010
CaEn-31	950	2.38×10^{5}	3.70×10^{-21}	−20.43	0.26	d	air	1990
CaEn-17	1000	7.56×10^{4}	1.58×10^{-20}	−19.80	0.12	b	air	1800
CaEn-15	1049	1.62×10^{4}	9.59×10^{-20}	−19.02	0.11	b	air	1810
CaEn-28	1050	1.80×10^{4}	2.87×10^{-20}	−19.54	0.17	b	NNO	3970
CaEn-29	1050	1.80×10^{4}	1.78×10^{-20}	−19.75	0.30	b	IW	1260
CaEn-34	1052	2.16×10^{4}	3.81×10^{-20}	−19.42	0.19	c	air	1350
CaEn-35	1052	2.16×10^{4}	4.92×10^{-20}	−19.31	0.18	d	air	1080
CaEn-13	1099	1.26×10^{4}	1.21×10^{-19}	−18.92	0.10	b	air	5600
CaEn-12	1150	5.40×10^{3}	1.62×10^{-19}	−18.79	0.15	b	air	2270
parallel to c								
CaEn-23	850	6.73×10^{5}	2.15×10^{-21}	−20.67	0.25	b	air	1490
CaEn-22	949	1.73×10^{5}	4.73×10^{-21}	−20.33	0.19	b	air	1340
CaEn-27	1050	2.16×10^{4}	3.01×10^{-20}	−19.52	0.14	b	air	2520

Sources: b – diopside + enstatite source; c – diopside + enstatite + qtz source; d – diopside + enstatite + forst source.
* Surface concentrations from fits to profiles with background concentration from naturally-present Ca substracted out.

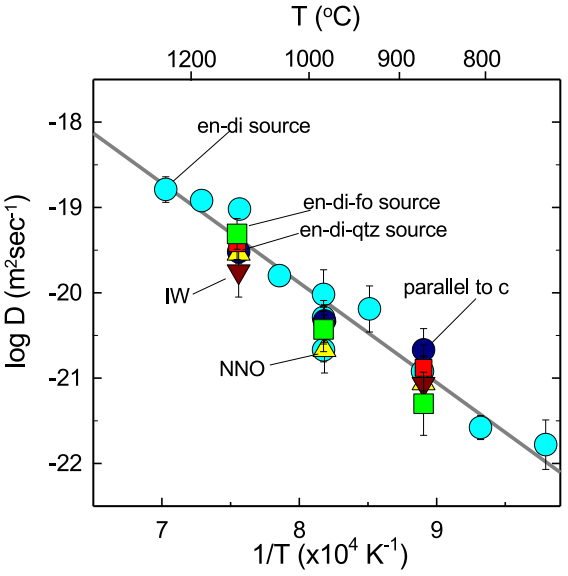

Fig. 2. Arrhenius plot of Ca diffusion data for enstatite. From a global fit to all of the data, we obtain an activation energy for diffusion of 240 ± 10 kJ mol^{-1} and pre-exponential factor of 1.17×10^{-10} m^2sec^{-1} (log $D_o = -9.93 \pm 0.42$). Ca diffusivities for transport normal to (210) and parallel to c in enstatite are similar, suggesting that anisotropy of Ca diffusion in orthopyroxene is not significant.

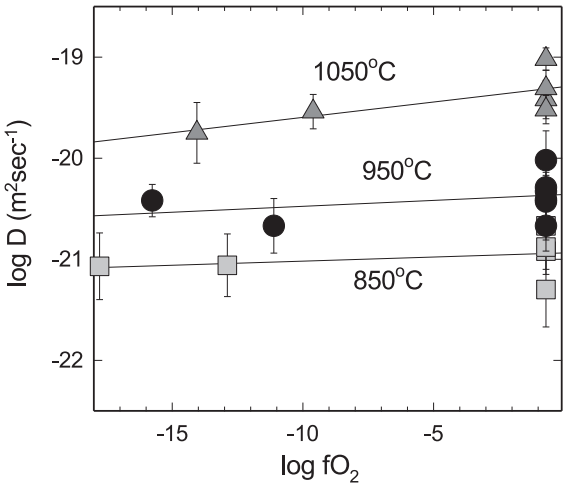

Fig. 3. Dependence of Ca diffusivities in enstatite on oxygen fugacity. At 1050 °C, the data show a small, weak dependence of Ca diffusion on fO_2, with a value of m of 0.034 ± 0.016.

work on Pb (Cherniak, 2001), REE (Cherniak and Liang, 2007) and Ti (Cherniak and Liang, 2012) diffusion across this temperature range suggests that it has little influence on measured diffusivities.

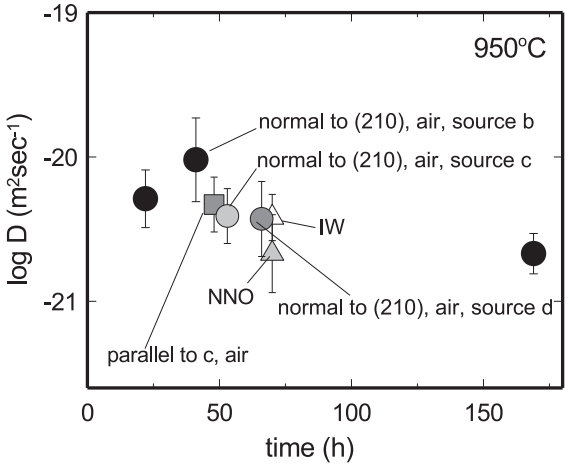

Fig. 4. Time-series study at 950 °C for experiments run in air with diffusion normal to the (210) cleavage face. Diffusivities are quite similar over times differing by about a factor of 8, suggesting that volume diffusion is the dominant process being measured. Also shown are diffusivities parallel to c, and diffusion for experiments run under IW-buffered and NNO-buffered conditions at this temperature, illustrating relative insensitivity to these parameters.

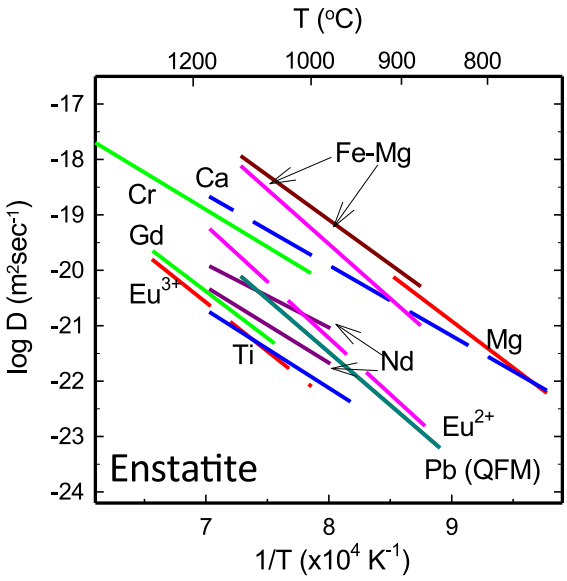

Fig. 5. Diffusion of various cations in enstatite. Sources for data: Mg – Schwandt et al. (1998); Fe-Mg – Dohmen et al. (2016); Cr – Ganguly et al. (2007); Eu, Gd – Cherniak and Liang (2007); Nd (IW) – Sano et al. (2011); Ti – Cherniak and Liang (2012). Ca diffusion is among the faster-diffusing species, within an order of magnitude of Mg, Cr, and Fe-Mg, and considerably faster diffusing than the trivalent REE, tetravalent Ti, and larger divalent cations Pb and Eu.

4.1. Cation diffusion in enstatite

Here we consider extant cation diffusion data in pyroxene with respect to our new results for Ca (Fig. 5). It is important to note that larger cations such as REE, Ca and Pb prefer the larger, irregular M2 site of pyroxene, whereas smaller cations such as Ti, Al, and Cr prefer the smaller, more regular M1 site of pyroxene. Mg and Fe^{2+} occupy both M1 and M2 sites. In the M2 site, cation coordination is eightfold in diopside and sixfold in enstatite, but sixfold for the M1 site in both pyroxenes. In the discussion below, we select effective ionic radius in view of this general observation.

The starting enstatite (from Embilipitiya, Sri Lanka) is the same and experimental approaches used in this work are similar to those used in our earlier studies of Ti (Cherniak and Liang, 2012), Pb (Cherniak, 2001) and REE diffusion in enstatite (Cherniak and Liang, 2007). Fig. 5 also compares results for Ca diffusion with those for Cr (Ganguly et al., 2007), Fe-Mg (Dohmen et al. 2016), Mg (Schwandt et al., 1998) and Nd (Sano et al., 2011). Overall, diffusivities show a dependence on both cation size and charge, and an apparent interplay between these two factors and dependence on M-site preference. Calcium diffusion is slower than Mg, Cr and Fe, but faster than larger divalent cations Pb and Eu that also are likely to preferentially occupy the M2 site (ionic radii of 1.00, 1.17 and 1.19 Å for Ca, Eu^{2+} and Pb in sixfold coordination, respectively; Shannon, 1976). Calcium diffusion is also faster than that for trivalent REE and tetravalent Ti. Interestingly, our measured activation energy for Ca diffusion in enstatite (240 ± 10 kJ/mol) is lower than those for Mg, Fe-Mg, and Eu^{2+} diffusion in enstatite or orthopyroxene, by 27–137 kJ/mol (Schwandt et al., 1998; Cherniak and Liang, 2007; Dohmen et al., 2016). Although diffusion is faster, activation energies for Fe-Mg diffusion in orthopyroxene are higher than Ca diffusion in enstatite (308 and 377 kJ/mol for $En_{91}Fs_9$ and $En_{99}Fs_1$, respectively, Dohmen et al., 2016).

When considering diffusion in other mineral phases with respect to our data, Ca diffusion in enstatite is intermediate in magnitude between Ca diffusion in clinopyroxene and olivine (Fig. 6), with Ca diffusion in enstatite about two orders of magnitude faster than Ca self-diffusion in diopside and two orders of magnitude slower than in olivine. This is consistent with the trend of Ca partitioning in the respective minerals, suggesting the importance of the size of the M2 site for Ca diffusion in pyroxene and olivine.

4.2. Dependence on silica activity and oxygen fugacity

Our measured Ca diffusivities are in agreement for the range of sources used in diffusion experiments. This suggests that there is little concentration dependence of Ca diffusion over the investigated range of conditions. Ca diffusion in enstatite also appears to have little dependence on silica activity of the diffusant source, given the similarities in Ca diffusivities for the various sources used in experiments.

Some cations in orthopyroxene exhibit pronounced dependences of diffusion on oxygen fugacity. Studies of Pb diffusion (Cherniak, 2001) indicate a positive dependence of diffusion on oxygen fugacity, suggesting that Pb

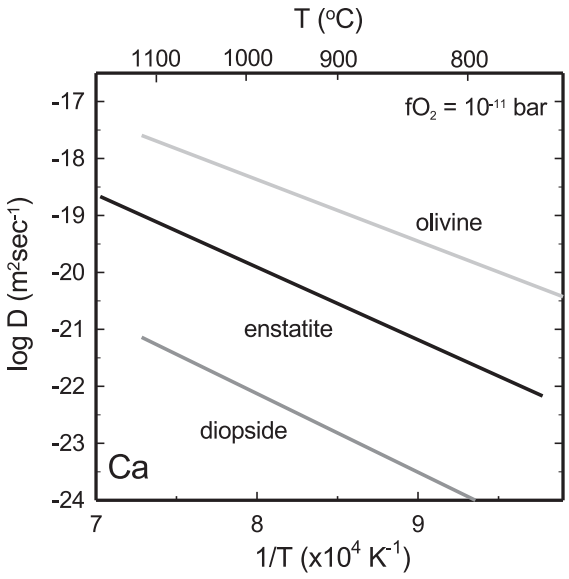

Fig. 6. Calcium diffusion in enstatite, olivine and diopside. For Ca diffusion in olivine and diopside, diffusivities are calculated for an oxygen fugacity of 10^{-11} bar and for diffusion parallel to c, using the diffusion parameters of Coogan et al (2005) and Dimanov and Jaoul (1998), respectively.

diffusion likely proceeds via a vacancy mechanism. The dependence found for Pb diffusion in enstatite, where $D_{Pb} \propto (pO_2)^m$ and m = 0.2, is similar to that for Pb diffusion in other pyroxenes investigated, and comparable to values determined for Fe diffusion in diopside (Azough and Freer, 2000). In contrast, Fe-Mg interdiffusion in orthopyroxene has at most a weak dependence on fO_2 (Dohmen et al., 2016), with m = 0.053 ± 0.027 for orthopyroxene of composition Fs_9, and no dependence on fO_2 for orthopyroxene with very low Fe content (Fs_1). Interestingly, the former value is similar to the dependence on fO_2 found for our Ca diffusion experiments at 1050 °C.

Dohmen et al. (2016) discussed diffusion mechanisms in pyroxene in terms of an fO_2-dependent transition metal extrinsic diffusion (TaMED) mechanism and an fO_2-independent pure extrinsic diffusion (PED) mechanism. In this model, vacancies in octahedral metal sites are charge balanced by trivalent cations, which may include aliovalent impurities such as Cr^{3+} or Al^{3+}, as well as Fe^{3+} created by Fe^{2+} oxidation, with the latter, but not the former, sensitive to fO_2. As fO_2 and Fe content of the material decrease, Fe^{3+} becomes less prevalent and charge balance by other species which lack dependence on fO_2 becomes more important. This represents a change in diffusion mechanism from a transition metal extrinsic diffusion mechanism, which is fO_2 dependent, to a pure extrinsic diffusion mechanism, which lacks dependence on fO_2 (Chakraborty, 1997; Dohmen et al., 2016). The enstatite in this work has very low amount of Al (0.047 a.p.f.u.) and Fe (0.016 a.p.f.u.). It is not clear if such low level of Al and Fe can support the transition metal extrinsic diffusion mechanism. The weak dependence of Ca diffusion in enstatite on fO_2 (Fig. 3) requires further study.

5. APPLICATIONS

The results obtained from this study can be used to understand diffusional loss or grain of Ca in orthopyroxene (opx) in natural samples. In this section we will briefly discuss some simple applications using these data. To highlight Ca diffusion in opx, we assume that opx grains are mineralogically homogeneous, i.e., without mineral inclusions and clinopyroxene exsolution lamellae. The latter will involve diffusion in other minerals in addition to opx. Without loss of generality, we use spherical geometry in the examples presented below.

5.1. Center retention times

We first consider the simple case of isothermal diffusive exchange, in which opx grains are spheres of radii a with an initial uniform concentration of diffusant C_1, exposed to an external medium with diffusant concentration C_0. This simple model also assumes that there is no external source or sink of Ca that could rate limit the exchange with the phase of interest. A solution to the diffusion equation at the center of a sphere with these initial and boundary conditions can be derived (e.g., Crank, 1975). When the dimensionless parameter Dt/a^2 (where D is the diffusion coefficient and t is the time) has a value less than or equal to 0.03, the concentration at the grain center will remain unchanged from its initial value. This may be referred to as the criterion for "center retention". When Dt/a^2 exceeds this value, the concentration of diffusant at the center of the grain will be affected by the external concentration C_0. In Fig. 7 curves for this condition are plotted as a function of tem-

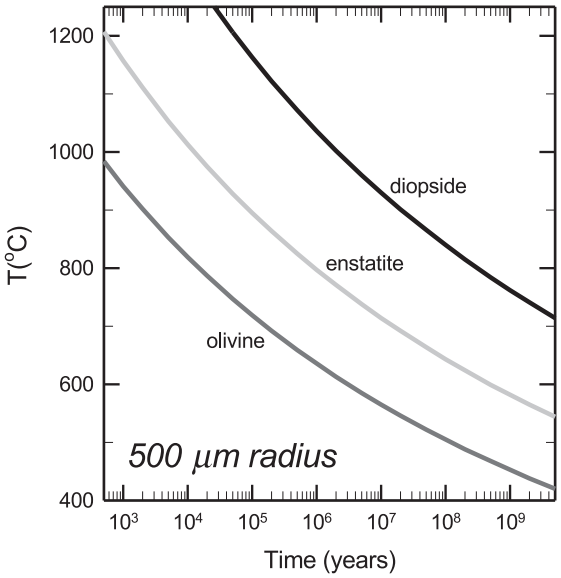

Fig. 7. Time temperature conditions for "center retention" of Ca isotopic or chemical signatures in the centers of 500 μm radius grains of enstatite, diopside and olivine for a simple case of isothermal heating. Diffusion parameters for olivine and diopside used in calculations are those plotted in Fig. 6. For conditions below each curve, compositions in the centers of grains are not altered by diffusion. See text for additional discussion.

perature and time for grains of radius 500 μm for Ca in olivine, enstatite and diopside, using the diffusion coefficients plotted in Fig. 6 for these minerals. While some diffusional anisotropy has been observed for Ca diffusion in olivine (Coogan et al., 2005) it is not large, so in these simple calculations we use parameters for diffusion parallel to c. The original Ca concentration and isotope signatures will be best retained in diopside, followed by enstatite and olivine. For example, at 800 °C, the original Ca signatures in mineral cores will be retained in enstatite for ~1 Myr, but for only 10,000 years in olivine, and over 500 Myr in diopside. At magmatic temperatures, such as 1200 °C, initial Ca concentration in the core of the 500 μm opx will be lost in less than 1000 years. This has important implications for the Ca-in-opx thermometer, which we will discuss below.

5.2. Closure temperature of the Ca-in-opx thermometer of Brey and Köhler (1990)

A practical application of the diffusion parameters obtained in this study is the closure temperature of the Ca-in-opx thermometer of Brey and Köhler (1990) which has been widely used to calculate equilibrium or closure temperatures of peridotites from different tectonic settings (e.g., orogenic, ophiolitic, and abyssal). The Ca-in-opx thermometer of Brey and Köhler (1990) is based on the temperature-dependent Ca solubility in opx buffered by clinopyroxene (cpx) and takes on the simple expression:

$$T(K) = \frac{6425 + 26.4P}{1.843 - \ln C_s} \quad (3)$$

where P is the pressure (in kbar); C_s is the Ca concentration or solubility in opx (in atoms per six oxygens in the pyroxene structure formulae or a.p.f.u.) coexisting with cpx. Rearranging Eq. (3), we have an expression for the temperature- and pressure-dependent Ca solubility in opx:

$$C_s = 6.3154\exp\left(-\frac{6425 + 26.4P}{T}\right). \quad (4)$$

The dependence of Ca solubility on pressure is relatively small. According to Eq. (4), Ca concentration in opx is 0.0899 (a.p.f.u.) at 1300 °C, 0.033 at 1000 °C, and 0.0124 at 800 °C, all at 10 kbar or 1 GPa. Hence during cooling, a fraction of Ca diffuses out of opx into adjacent cpx.

The Ca-in-opx thermometer of Brey and Köhler (1990) is calibrated for four-phase spinel- or garnet-lherzolites of mantle-like compositions, i.e., Mg# (=100 Mg/Mg + Fe, in molar) of opx and cpx around 90. There is no Ca diffusion data for mantle-like opx. In Cherniak and Liang (2012), we measured Ti diffusion in natural opx in a spinel lherzolite xenolith from Kilbourne Hole, New Mexico and the same batch of enstatite used in the present study. We found that Ti diffuses slightly faster in the enstatite than the natural opx (by a factor of 1.3 at 1200 °C and 2.1 at 800 °C). Unless Fe has a strong preference for substituting for Ca in the M2 site of opx, we expect a small difference in Ca diffusivity for the enstatite and mantle-like opx. Hence, to a good approximation, our measured Ca diffusion parameters can be used to assess diffusional loss/gain of Ca in mantle-like opx. Fig. 8a presents an example of calculated Ca concentration profiles for a spherical opx grain of 1 mm radius subjected to a prescribed cooling. The cooling function follows that of Dodson (1973):

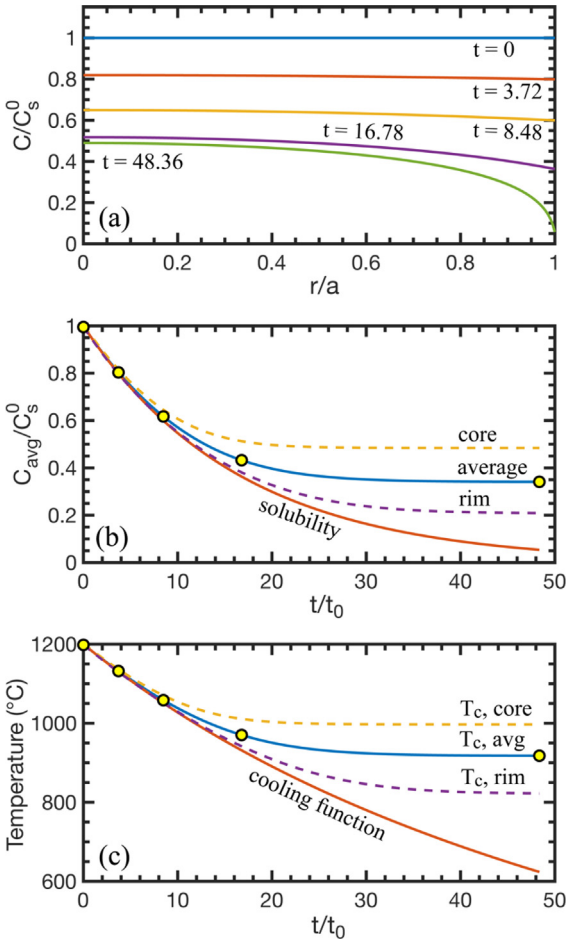

Fig. 8. (a) An example of calculated Ca diffusion profiles at 5 selected times in a 1 mm spherical opx grain and at a cooling rate of 200 °C/Myr. (b) Variations of the average concentration (blue curve), core and rim concentrations (dashed curves), and the Ca solubility in opx (red curve, Eq. (3)) as a function of time. (c) Variations of calculated temperatures based on the average, core, and rim Ca concentrations as a function of time. The 5 filled circles correspond to the 5 diffusion profiles in (a). The radial distance (r) is normalized by grain radius. The closure temperature is calculated using the method of Dodson (1975) and Yao and Liang (2015). The cooling curve in (b) is based on Eqs. 4a and 4b with T_c = 918 °C. The time is scaled by diffusion time at 1200 °C. A unit time is 63.98 kyr. The concentrations in (a) and (b) are scaled by the initial Ca concentration in opx at 1200 °C. The diffusion profiles are for a spherical geometry, calculated using a variable time-step finite difference method and Eq. (3) as the boundary condition. (For interpretation of the references to color in this figure legend, the reader is referred to the web version of this article.)

$$\frac{1}{T} = \frac{1}{T_0} + \eta t, \eta = \frac{\dot{s}}{T_c^2}, \quad (5a, 5b)$$

where T_0 is the starting temperature (1200 °C in this example); and $\dot{s}$ is the cooling rate (200 °C/Myr) at temperature T_c. Initially the opx grain is well-equilibrated at 1200 °C

and 1 GPa. In the presence of cpx, Ca concentration in the outmost rim of opx is given by Eq. (4) at temperature T. The closure profile for Ca is established after 38 time units or 2.4 Myr in this example. Fig. 8b shows that the grain-averaged Ca concentration decreases gradually as a function of time, and approaches an asymptotic value of 0.34 times of the initial Ca in opx after 2.4 Myr. The system is effectively closed to Ca diffusional loss thereafter. The temperature that corresponds to the cessation of diffusional loss of Ca from opx is the closure temperature of the Ca-in-opx thermometer. Following Dodson (1976) and Yao and Liang (2015), the closure temperature for the Ca-in-opx thermometer can be obtained by substituting the asymptotic value of the average Ca concentration into Eq. (3), which gives a temperature of 918 °C at 1 GPa for the present example. Graphically, this is equivalent to first finding a closure time by projecting the asymptotic value of the average Ca concentration to the solubility curve in Fig. 8b. The closure temperature is obtained by projecting the closure time to the cooling function curve in Fig. 8c. (For an illustrated example, a reader is referred to Fig. 3 in Yao and Liang, 2015.) Fig. 8c shows that the temperature calculated by substituting the average Ca concentration into Eq. (4) decreases gradually as a function of time, and approaches the asymptotic value or closure temperature of 918 °C after 2.4 Myr. The graphic method illustrated in Fig. 8a-8c can be quantified by a modified Dodson's equation for closure temperature with the Ca-in-opx thermometer of Brey and Köhler (1990) as the boundary condition (Eq. (4)).

Dodson (1973) derived the now-familiar expression for closure temperature (T_c):

$$\frac{E_a}{RT_c} = \ln\left(\frac{ART_c^2 D_0}{E_a \dot{s} a^2}\right), \tag{6}$$

where E and D_0 are the activation energy and pre-exponential factor for diffusion of the element of interest; $\dot{s}$ is the cooling rate at the closure temperature; a is the effective diffusion radius; R is the gas constant; and A is a geometric factor and is equal to 55 for a spherical mineral grain. Fig. 9a compares closure temperatures of the Ca-in-opx thermometer of Brey and Köhler (1990) calculated using a finite difference method with Eq. (4) as the boundary condition (open symbols) with closure temperatures calculated using Dodson's equation (solid lines) for a range of grain sizes (0.04–10 mm) and cooling rates (2–2000 °C/M yr). For the grain size and cooling rate considered here, the closure temperatures of the Ca-in-opx thermometer are 10–30 °C higher than the closure temperatures based on Dodson's equation (for details see supplementary Fig. S2). This is due to the difference in boundary conditions between the two models. In Dodson's model, the concentration of Ca at the opx surface decreases linearly as a function of time, whereas in the Ca-in-opx thermometer of Brey and Köhler (1990), the concentration of Ca at the opx surface decreases exponentially as a function of time (Eq. (4)). The latter is shown as the solubility curve in Fig. 8b. The deceleration of Ca solubility at lower temperature and later time (e.g., $t/t_0 > 15$ in Fig. 8b) hinders more efficient Ca diffusional loss compared to the case of a linear solubility. Consequently, more Ca is retained in the case of the exponential time-dependent boundary condition (Eqs. (4) and (5)) than the linear time-dependent one. The higher average concentration in the former case leads to a higher closure temperature for the Ca-in-opx thermometer. The dependence of closure temperature on element solubility or the "equilibrium concentration-temperature relationship" at the mineral surface was pointed out by Dodson (1986) and demonstrated numerically by Yao and Liang (2015) for both linear and exponential temperature-dependent solubility relationships. The systematic differences in closure temperature between the two choices of solubility functions can be accounted for by adjusting the geometric constant A in Eq. (6). Based on results of numerical simulations, we find that A depends weakly on the product of cooling rate and grain size squared. To a good approximation, a constant value of $A = 35.91 \pm 0.10$ can reproduce the numerically derived closure temperatures for the Ca-in-opx thermometer of Brey and Köhler (1990) very well. This is shown in Fig. 9a where the dashed lines are calculated from Eq. (6) with $A = 35.91$. The smaller geometric constant A is especially significant when the cooling rate is high and grain size is large. For example, for an opx radius of 1 mm and cooling rates of 0.02 °C/yr, 0.2 °C/yr, and 2 °C/yr, the closure temperatures for the Ca-in-opx thermometer (Eq. (6) with $A = 35.91$) are 54, 72, and 100 °C higher than the respective closure temperatures derived from Dodson's equation with $A = 55$.

In most petrologic studies of mantle samples, concentrations of Ca in opx are measured by spot analysis using an electron probe microanalyzer (EPMA). Very often, both core and rim compositions, obtained by local averaging of several spot analyses, are reported in the literature. Application of the Ca-in-opx thermometer of Brey and Köhler (1990) to the local averaged Ca concentrations then can lead to two calculated temperatures, with the core temperature being higher than the rim temperature. Fig. 8b presents an example of calculated Ca concentrations averaged over spherical regions of $r/a = 0$–0.2 (core) and $r/a = 0.9$–1 (rim). The corresponding closure temperatures are 998 and 820 °C, respectively (Fig. 8c). Depending on grain size and cooling rate, the closure temperatures calculated from the central region of opx are 100–300 °C higher than closure temperatures derived from Ca concentrations in the near rim region (Fig. 10a). Fig. 9b shows that the core, middle ($r/a = 0.6$–0.8), and rim closure temperatures for the Ca-in-opx thermometer of Brey and Köhler (1990) can be well reproduced by Eq. (5) with the following geometric constants: $A = 6.38 \pm 0.12$ (core), $A = 17.71 \pm 0.13$ (mid), and $A = 408 \pm 10$ (rim). The smaller difference in closure temperature or parameter A between the core and the middle regions is due to the r-cubed effect, as $r/a = 0.8$ only encloses 51% of the spherical volume. Figures similar to Fig. 9b but with cooling rates of 2, 20, and 2000 °C/Myr are presented in supplementary (Fig. S3.

Fig. 10b compares closure temperatures for the Ca-in-opx thermometer of Brey and Köhler (1990) calculated using Ca concentrations in the core (T_{core}) and rim (T_{rim}) of opx. For the ranges of grain size and cooling rate shown

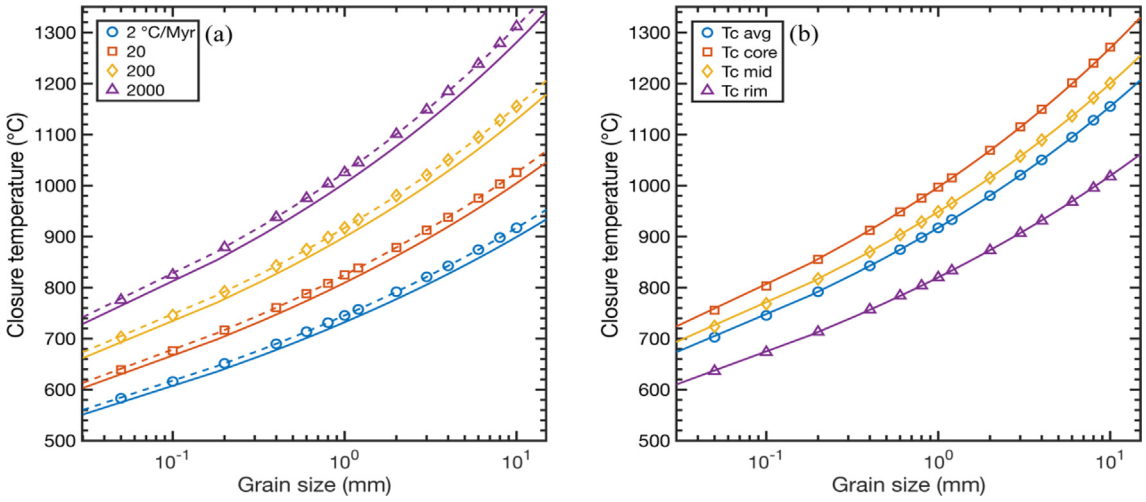

Fig. 9. (a) Comparison of closure temperatures for the Ca-in-opx thermometer of Brey and Köhler (1990) (symbols) with closure temperatures based on Dodson's equation for a spherical grain (solid lines, Eq. (5) with A = 55). The symbols are the closure temperatures for the Ca-in-opx thermometer of Brey and Köhler (1990) calculated numerically for a range of grain sizes and four choices of cooling rates. The dashed lines are calculated using Eq. (5) with A = 36.19. (b) Closure temperatures for the Ca-in-opx thermometer of Brey and Köhler (1990) (symbols) based on the average Ca in opx (avg), in the core region (r/a = 0–0.2), the middle shell (mid, r/a = 0.6–0.8), and the outermost shell or rim (r/a = 0.9–1) for a cooling rate of 200 °C/Myr. The solid lines in (b) are calculated using Eq. (5) but with A = 35.91 (avg), A = 6.38 (core), A = 17.71 (mid), and A = 408 (rim), respectively. Figures similar to (b) but for cooling rates of 2, 20, and 2000 °C/Myr are presented in supplementary Fig. S2.

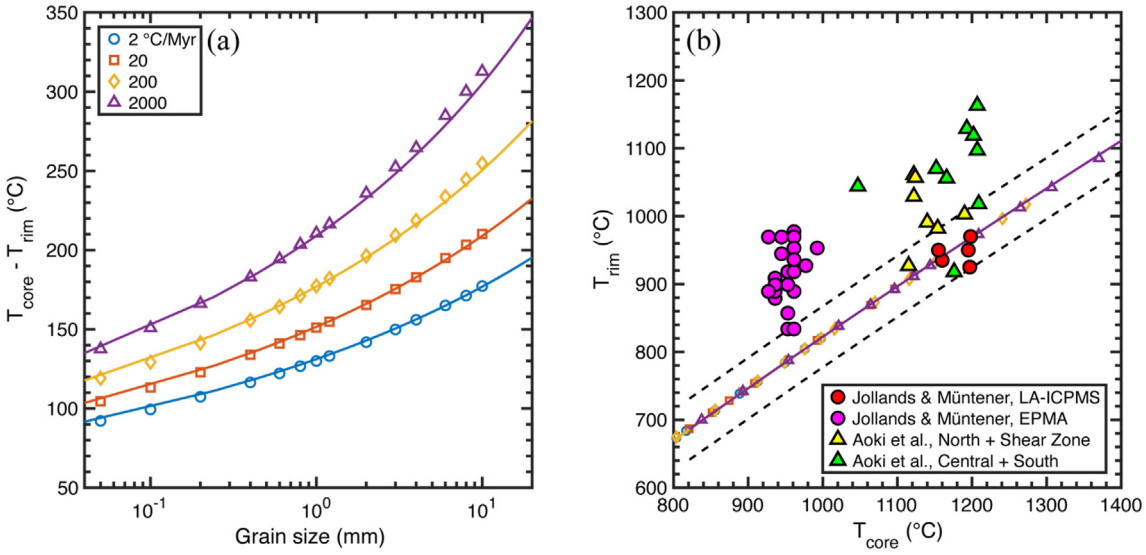

Fig. 10. (a) Differences in core- and rim-derived closure temperatures for the Ca-in-opx thermometer of Brey and Köhler (1990) for a range of grain size and cooling rates. The symbols represent closure temperatures for the Ca-in-opx thermometer calculated numerically. The solid lines are calculated core and rim temperatures using Eq. (5) with A = 6.38 (core, r/a = 0–0.2) and A = 408 (rim, r/a = 0.9–1), respectively. (b) Correlations between core- and rim-derived closure temperatures for the Ca-in-opx thermometer of Brey and Köhler (1990). The open symbols and solid lines are the same as those in (a). Dashed lines are ±45 °C from the solid lines. Color-filled circles and triangles are closure temperatures based in Ca concentrations in the core and rim of opx in plagioclase lherzolites from the Lanzo massif (Jollands and Müntener, 2019; Aoki et al., 2020). See text for discussion.

in Fig. 10a, the core and rim closure temperatures fall on a single curve, referred to as the closure curve hereafter. The shape and location of the closure curve depend on the activation energy for Ca diffusion in opx, but are independent of the pre-exponential factor for diffusion, cooling rate, and opx grain size. This can be shown by applying Eq. (5) to the core and rim closure temperatures, respectively. Subtracting the two resulting closure temperature equations, we have:

$$T_{c,rim} = \frac{T_{c,core}}{1 - \frac{RT_{c,core}}{E_a} \ln \frac{A_{core}}{A_{rim}}}, \quad (7)$$

where the term s in $T_c^2/\dot{s}a^2$ Eq. (6) is cancelled out for the simple cooling history described by Eq. (6) in which the cooling parameter η is a constant. If the cooling history of a set of peridotite samples follows that of Eq. (5) and our measured activation energy for Ca diffusion in enstatite is applicable to natural opx, temperatures calculated using Ca concentrations in the core and rim of opx and the Ca-in-opx thermometer of Brey and Köhler (1990) should be related to each other via the closure curve or Eq. (7). This is the case for a number of plagioclase peridotites from the Lanzo Massif, northern Italy (Fig. 10b).

5.3. Thermal history of peridotites based on closure temperatures of Ca in orthopyroxene

Aoki et al. (2020) presented a detailed study of mineral major element compositional variations in 16 plagioclase peridotites from the four units of the Lanzo peridotite (North, Shear zone, Central and South). They showed that temperatures calculated using Ca concentrations in the cores of opx grains are generally higher than those in the rims of opx (yellow and green triangles in Fig. 10b). However, majority of their samples (11 out of the 16) have significantly higher-than-expected T_{rim}, by >45 °C compared to those predicted by Eq. (7). The higher-than-expected T_{rim} is likely due to the presence of cpx exsolution lamellae, which may hinder Ca diffusion through the host opx and which may be accidentally included in spot analysis by EPMA. Jollands and Müntener (2019) examined the latter hypothesis by carefully avoiding cpx exsolution lamellae using a focused beam in their EPMA measurements of major element concentration profiles in selected opx grains in six samples from the North, Shear Zone, and Central units of the Lanzo Massif. Temperatures based on their reported core and rim Ca concentrations are shown as magenta circles in Fig. 10b. By excluding cpx lamellae, the Ca-in-opx core temperatures are significantly reduced compared to samples from similar units of Aoki et al. (2020, yellow triangles in Fig. 10b). As there are less cpx exsolution lamellae in the opx rim region (Jollands and Müntener, 2019; Aoki et al., 2020), the EPMA-derived rim temperatures of the six samples are comparable to or slightly lower than those of Aoki et al. (2020). To calculate a temperature before cpx exsolution, Jollands and Müntener (2019) used laser-ablation inductively coupled plasma mass spectrometry (LA-ICPMS) and a large beam spot (100 μm) to measure the average opx core composition, and EPMA with focused beam to characterize opx rim composition. Fig. 10b shows that their LA-ICPMS + EMPA derived core and rim Ca-in-opx temperatures are plotted on or very close to the closure curve defined by Eq. (7). This provides an independent test of our measured activation energy for Ca diffusion in enstatite. Interestingly, the LA-ICPMS-derived core temperatures are within the range of core temperatures reported by Aoki et al. (2020). Given the concordant core and rim temperatures, it is possible to obtain self-consistent cooling rates and cooling parameters (η in Eq. (5)). Based on the average grain size for each of the five samples from Jollands and Müntener (2019), we found cooling rates of 10–100 °C/Myr at the closure temperatures recorded by Ca concentrations in the opx cores. The corresponding cooling parameters are $\log(\eta) = -17.6$ to -18.7 (in $K^{-1}s^{-1}$). These cooling rates and cooling parameters are in good agreement with those reported by Jollands and Müntener (2019) based on diffusion modeling of Cr concentration profiles in opx and Aoki et al. (2020) based on diffusion modeling of Ca profiles in olivine.

5.4. Thermal history of peridotites based on closure temperatures of Ca and REE in orthopyroxene

For two elements in opx, their closure temperatures are correlated via Eq. (6), defining a closure curve in the closure temperature vs. closure temperature diagram. Here we consider closure temperatures of Ca and REE in opx in peridotites. The partitioning of REE between opx and cpx in peridotites depends primarily on temperature and pyroxene major element compositions, which can be used as a thermometer (Witt-Eickschen and O'Neill, 2005; Lee et al., 2007; Liang et al., 2013). Based on diffusion parameters of Van Orman et al. (2001) and Cherniak and Liang (2007) for REE diffusion in diopside and enstatite, Liang (2015) and Yao and Liang (2015) showed that closure temperatures of the REE-in-two-pyroxene thermometer of Liang et al. (2013, designated as T_{REE}) are essentially the same as closure temperatures of REE in opx in the same two pyroxenes system, unless cpx abundance in the peridotite is very low. Dygert et al. (2017) documented systematic variations in temperatures calculated using REE- and major element-based thermometers as a function of stratigraphic location from the crust-mantle boundary in the mantle section of the Oman ophiolite. For a given thermometer, the calculated temperatures decrease from the crust-mantle boundary into the mantle (see their Fig. 2). Fig. 11a compares their calculated temperatures, based on Ca in opx and REE partitioning between opx and cpx (circles). As expected, slower diffusion of REE in opx (Fig. 5) gives rise to higher closure temperatures of the REE than those of Ca in opx. Except for two samples that have the lowest T_{REE} and are located farthest from the crust-mantle boundary, the calculated temperatures for the remaining six samples are within the range bracketed by the predicted core and rim closure temperatures for Ca in opx (dash and dash-dotted lines). The two samples with higher-than-expected $T_{Ca\text{-}in\text{-}opx}$ in the lower end of T_{REE} in Fig. 11a may be affected by cpx exsolution. According to Dygert et al. (2017), sample OM94-98 (red circle in Fig. 11a) has a low bulk Ca content and has small cpx grains in large opx host. These authors postulated that cpx in this sample might have exsolved from the host opx at lower temperatures. This is consistent with the predicted opx rim temperature in Fig. 11a. Given the closure temperatures of Ca and REE in opx and opx grain sizes, we can calculate cooling rates using Eq. (5). The results are shown in Fig. 11b and c. The cooling rates are 5–50 °C/Kyr for the three samples closer to the crust-mantle boundary (green circles) and 0.05–2 °C/Kyr for the four samples far away. These are in very good agreement the results of Dygert et al. (2017) who used closure curves established by T_{REE}

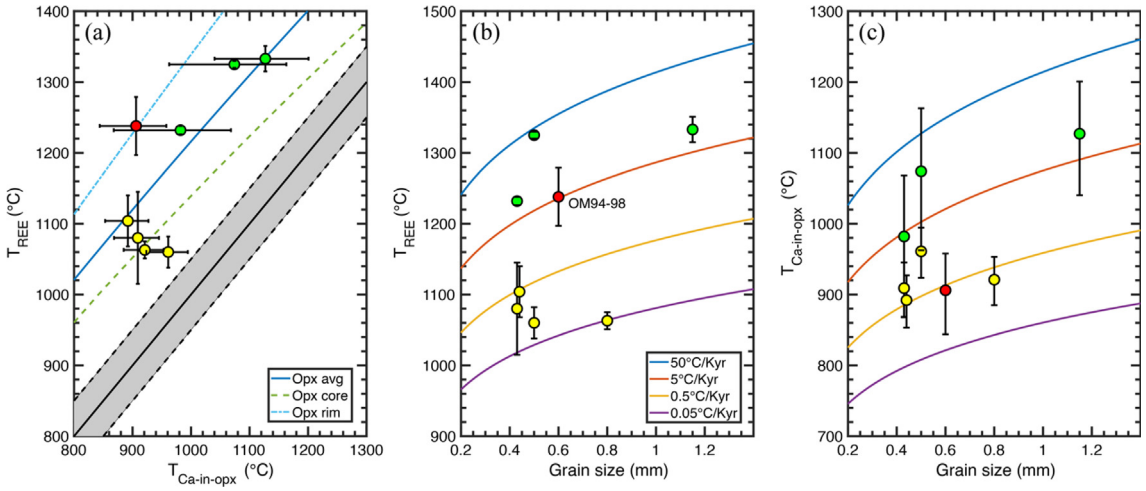

Fig. 11. (a) Comparison of closure temperatures of Ca and REE in opx in eight harzburgite samples from the Oman ophiolite (circles, data from Dygert et al., 2017). The closure temperatures are calculated using the Ca-in-opx thermometer of Brey and Köhler (1990) and the REE-in-two-pyroxene thermometer of Liang et al. (2013). The solid, dashed, and dash-dotted lines are closure temperatures of Ca in opx based on the average, core, and rim concentrations. (b) and (c) Variations of REE and Ca closure temperatures as a function of opx grain size for the Oman samples. Curves of constant cooling rates are shown as solid lines. Green and yellow circles are samples closer (≤2.15 km) and far away (>4 km) from the crust-mantle boundary, respectively. One sample (red circle, OM94-98), according to Dygert et al. (2017), was a cpx-free harzburgite at high temperatures. See text for discussion. (For interpretation of the references to color in this figure legend, the reader is referred to the web version of this article.)

and temperatures derived from the two-pyroxene thermometer of Brey and Köhler (1990) to estimate the cooling rate.

6. SUMMARY AND FURTHER DISCUSSION

Ca diffusivities measured in natural enstatite in this study under buffered conditions (IW, NNO) and in air indicate little dependence on oxygen fugacity. Experiments conducted with a variety of sources of diffusant indicate little dependence on silica activity or Ca concentrations in the diffusant source over the range of conditions investigated. In addition, there appears to be little anisotropy of Ca diffusion in enstatite. Diffusion parameters for the Arrhenius equation for Ca diffusion in enstatite were obtained (Eqs. (1) and (2)) and compared with extant data for cation diffusion in opx. We found that Ca diffusion in enstatite is faster than that for larger divalent cations Pb and Eu and faster than diffusion of trivalent REE and tetravalent Ti, but slower than Mg, Cr and Fe. More work is needed to fully characterize the dependence of Ca diffusion on opx composition and fO_2. When compared with diffusivities in other minerals, Ca diffusion in enstatite is about two orders of magnitude faster than Ca self-diffusion in diopside and two orders of magnitude slower than Ca diffusion in olivine. The latter also explains the lower closure temperatures derived from the Ca-in-olivine thermometers than those from the Ca-in-opx thermometer for peridotite samples (e.g., Dygert et al., 2017; Aoki et al., 2020).

In addition to diffusion parameters, cooling rate, and effective grain size, closure temperature of an element in a mineral also depends on its solubility. A simple Dodson-like model for the closure temperature of the Ca-in-opx thermometer of Brey and Köhler (1990) has been developed using Ca diffusion data obtained from this study (Eq. (5)). The model has the same mathematical form as Dodson's equation but with different geometric constants (A) to account for the exponential temperature dependent Ca solubility in opx buffered by cpx (Eq. (3)). The closure temperature of the Ca-in-opx thermometer is significantly higher than the closure temperature based on Dodson's equation when the cooling rate is high and opx grain size is large. Initial applications of the simple model to peridotites from the Lanzo Massif and the Oman ophiolite have demonstrated the advantages of using closure curves established by the core and rim temperatures derived from Ca and REE solubilities in opx to constrain thermal history experienced by the peridotites. There are, however, potential complications arising from cpx exsolution lamellae.

The simple closure temperature equation (Eq. (5)) and its applications presented in this study are valid if diffusion of Ca in cpx lamellae is not the rate-limiting factor for Ca diffusion through the opx grain. This assumption is likely reasonable when the width of cpx lamella is very thin compared to the size of opx grain, which is the case for at least some of the Lanzo opx reported by Jollands and Müntener (2019, see their Fig. 2). However, when the cpx lamella is thicker, the slow diffusion of Ca in cpx may act to hinder Ca diffusional loss from opx, resulting in higher-than-expected Ca-in-opx core temperatures. The simple closure temperature equations such as the ones presented in this study are not applicable to those more complicated cases.

DECLARATION OF COMPETING INTEREST

The authors declare that they have no known competing financial interests or personal relationships that could have appeared to influence the work reported in this paper.

ACKNOWLEDGEMENTS

We thank Bruce Watson, Mike Jollands, and Nick Dygert for valuable discussion during the course of this work. We also thank two anonymous reviewers and Associate Editor James Van Orman for their constructive comments on the manuscript. This work was supported by NSF grants EAR-1632815 and OCE-1852088.

APPENDIX A. SUPPLEMENTARY MATERIAL

Supplementary material to this article can be found online at https://doi.org/10.1016/j.gca.2022.06.018.

REFERENCES

Aoki T., Ozawa K., Bodinier J.-L., Boudier F. and Sato Y. (2020) Thermal and decompression history of the Lanzo Massif, northern Italy: implications for the thermal structure near the lithosphere-asthenosphere boundary. *Lithos* **372–373**, 105661.

Azough F. and Freer R. (2000) Iron diffusion in single-crystal diopside. *Phys. Chem. Mineral.* **27**, 732–740.

Brey G. and Köhler T. (1990) Geothermobarometry in four-phase lherzolites II. New thermobarometers, and practical assessment of existing thermobarometers. *J. Petrol.* **31**, 1353.

Chakraborty S. (1997) Rates and mechanisms of Fe-Mg interdiffusion in olivine at 980°C–1300°C. *J. Geophys. Res.* **102**, 12317–12331.

Cherniak D. J. (1998) Pb diffusion in clinopyroxene. *Chem. Geol.* **150**, 105–117.

Cherniak D. J. (2001) Pb diffusion in Cr diopside, augite, and enstatite, and consideration of the dependence of cation diffusion in pyroxene on oxygen fugacity. *Chem. Geol.* **177**, 381–397.

Cherniak D. J. and Liang Y. (2007) Rare earth element diffusion in natural enstatite. *Geochim. Cosmochim. Acta* **71**, 1324–1340.

Cherniak D. J. and Liang Y. (2012) Ti diffusion in natural pyroxene. *Geochim. Cosmochim. Acta* **98**, 31–47.

Cherniak D. J. and Watson E. B. (1992) A study of strontium diffusion in K-feldspar, Na-K feldspar and anorthite using Rutherford Backscattering Spectroscopy. *Earth Planet. Sci. Lett.* **113**, 411–425.

Cherniak D. J. and Watson E. B. (1994) A study of strontium diffusion in plagioclase using Rutherford Backscattering Spectroscopy. *Geochim. Cosmochim. Acta* **58**, 5179–5190.

Coogan L., Hain A., Stahl S. and Chakraborty S. (2005) Experimental determination of the diffusion coefficient for calcium in olivine between 900°C and 1500°C. *Geochim. Cosmochim. Acta* **69**, 3683–3694.

Crank J. (1975) *The Mathematics of Diffusion*, Second ed. Oxford, p. 414.

Dimanov A. and Ingrin J. (1995) Premelting and high-temperature diffusion of calcium in synthetic diopside: an increase of the cation mobility. *Phys. Chem. Mineral.* **22**, 437–442.

Dimanov A and Jaoul O (1998) Calcium self-diffusion in diopside at high temperature: implications for transport properties.. *Phys. Chem. Minerals* **26**, 116–127.

Dimanov A., Jaoul O. and Sautter V. (1996) Calcium self-diffusion in natural diopside single crystals. *Geochim. Cosmochim. Acta* **60**, 4095–4106.

Dodson M. H. (1973) Closure temperature in cooling geochronological and petrological systems. *Contrib. Miner. Petrol.* **40**, 259–274.

Dodson M. H. (1976) Kinetic processes and thermal history of slowly cooling solids. *Nature* **259**, 551–553.

Dodson M. H. (1986) Closure profiles in cooling systems. *Mat. Sci. Forum* **7**, 145–154.

Dohmen R., Ter heege J. H., Becker H.-W. and Chakraborty S. (2016) Fe-Mg interdiffusion in orthopyroxene. *Am. Mineral.* **101**, 2210–2221.

Dygert N. J., Kelemen P. and Liang Y. (2017) Spatial variations in cooling rate in the mantle section of the Samail ophiolite in Oman: implications for formation of lithosphere at mid-ocean ridges. *Earth Planet. Sci. Lett.* **465**, 134–144.

Ganguly J. and Tazzoli V. (1994) Fe^{2+}-Mg interdiffusion in orthopyroxene: retrieval from the data on intracrystalline exchange reaction. *Am. Min.* **79**, 930–937.

Ganguly J., Ito M. and Zhang X. (2007) Cr diffusion in orthopyroxene; experimental determination, ^{53}Mn- ^{53}Cr thermochronology, and planetary applications. *Geochim. Cosmochim. Acta* **71**, 3915–3925.

Jollands M. C. and Müntener O. (2019) Testing orthopyroxene diffusion chromometry on rocks from the Lanzo Massif (Italian Alps). *J. Geophys. Res. Solid Earth* **124**, 7822–7841.

Lee C. T. A., Harbert A. and Leeman W. P. (2007) Extension of lattice strain theory to mineral/mineral rare-earth element partitioning: an approach for assessing disequilibrium and developing internally consistent partition coefficients between olivine, orthopyroxene, clinopyroxene and basaltic melt. *Geochim. Cosmochim. Acta* **71**, 481–496.

Liang Y. (2015) Simple models for closure temperature of a trace element in cooling bi-mineralic systems. *Geochim. Cosmochim. Acta* **165**, 35–43.

Liang Y., Sun C. and Yao L. (2013) A REE-in-two-pyroxene thermometer for mafic and ultramafic rocks. *Geochim. Cosmochim. Acta* **102**, 246–260.

Lindsley D. H. (1983) Pyroxene thermometry. *Am. Mineral.* **68**, 477–493.

Nimis P. and Grütter H. (2010) Internally consistent geothermometers for garnet peridotites and pyroxenites. *Contrib. Miner. Petrol.* **159**, 411–427.

Ozawa K. (2004) Thermal history of the Horoman Peridotite Complex: a record of thermal perturbation in the lithospheric mantle. *J. Petrol.* **45**, 253–273.

Sano J., Ganguly J., Hervig R., Dohmen R. and Zhang X. (2011) Neodymium diffusion in orthopyroxene: experimental studies and applications to geological and planetary problems. *Geochim. Cosmochim. Acta* **75**, 4684–4698.

Schwandt C. S., Cygan R. T. and Westrich H. R. (1998) Magnesium self-diffusion in orthoenstatite. *Contrib. Miner. Petrol.* **130**, 390–396.

Shannon R. D. (1976) Revised effective ionic radii and systematic studies of interatomic distances in halides and chalcogenides. *Acta Cryst.* **A32**, 751–767.

Sneeringer M., Hart S. R. and Shimizu N. (1984) Strontium and samarium diffusion in diopside. *Geochim. Cosmochim. Acta* **48**, 1589–1608.

Takazawa E., Frey F., Shimizu N. and Obata M. (1996) Evolution of the Horoman Peridotite (Hokkaido, Japan): implications from pyroxene compositions. *Chem. Geol.* **134**, 3–26.

Van Orman J. A., Grove T. L. and Shimizu N. (2001) Rare earth element diffusion in diopside; influence of temperature, pressure, and ionic radius, and an elastic model for diffusion in silicates. *Contrib. Miner. Petrol.* **141**, 687–703.

Witt-Eickschen, G., 2007. Thermal and geochemical evolution of the shallow subcontinental lithospheric mantle beneath the Eifel: constraints from mantle xenolith, a review. In: Ritter, J.R.R., Christensen, U. R. (Eds.), Mantle Plumes, pp. 323–337.

Witt-Eickschen G. and O'Neill H. S. C. (2005) The effect of temperature on the equilibrium distribution of trace elements

between clinopyroxene, orthopyroxene, olivine and spinel in upper mantle peridotite. *Chem. Geol.* **221**, 65–101.

Witt-Eickschen G. and Seck H. A. (1991) Solubility of Ca and Al in orthopyroxene from spinel peridotite: an improved version of an empirical geothermometer. *Contrib. Miner. Petrol.* **106**, 431–439.

Yao L. and Liang Y. (2015) Closure temperature in cooling bi-mineralic systems: I. Definition and with application to REE-in-two-pyroxene thermometer. *Geochim. Cosmochim. Acta* **162**, 137–150.

Associate editor: James Van Orman